



## Radar Attenuation in Enceladus' Ice Shell: Obstacles and Opportunities for Constraining Shell Thickness, Chemistry, and Thermal Structure

## Key Points:

- We explore radar attenuation within Enceladus' ice shell as a function of its chemistry using a 3D model of its shape and thermal structure
- Direct radar detection of the ice-ocean interface is improbable for chloride-rich shells except for the thin south-polar region
- The NH<sub>3</sub> eutectic isotherm is a comparatively easy-to-detect interface, with the potential to constrain the shell thickness and composition

## Correspondence to:

O. Souček,  
[ondrej.soucek@mff.cuni.cz](mailto:ondrej.soucek@mff.cuni.cz)

## Citation:

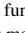





Souček, O., Běhounková, M., Schroeder, D. M., Wolfenbarger, N. S., Kalousová, K., Steinbrügge, G., & Soderlund, K. M. (2023). Radar attenuation in Enceladus' ice shell: Obstacles and opportunities for constraining shell thickness, chemistry, and thermal structure. *Journal of Geophysical Research: Planets*, 128, e2022JE007626. <https://doi.org/10.1029/2022JE007626>

Received 17 OCT 2022

Accepted 31 JAN 2023

Corrected 3 MAR 2023

This article was corrected on 3 MAR 2023. See the end of the full text for details.

Ondřej Souček<sup>1</sup> , Marie Běhounková<sup>2</sup> , Dustin M. Schroeder<sup>3,4</sup> , Natalie S. Wolfenbarger<sup>5</sup> , Klára Kalousová<sup>2</sup> , Gregor Steinbrügge<sup>6</sup>, and Krista M. Soderlund<sup>5</sup> 

<sup>1</sup>Mathematical Institute, Faculty of Mathematics and Physics, Charles University, Prague, Czech Republic, <sup>2</sup>Department of Geophysics, Faculty of Mathematics and Physics, Charles University, Prague, Czech Republic, <sup>3</sup>Department of Geophysics, Stanford University, Stanford, CA, USA, <sup>4</sup>Department of Electrical Engineering, Stanford University, Stanford, CA, USA, <sup>5</sup>Institute for Geophysics, Jackson School of Geosciences, University of Texas at Austin, Austin, TX, USA, <sup>6</sup>Jet Propulsion Laboratory, California Institute of Technology, Pasadena, CA, USA

**Abstract** Enceladus is a dynamic icy moon of Saturn and a leading target for future planetary missions focused on the search for life beyond Earth. For such missions, instruments that can provide geophysical and geochemical context for ice shell and ocean processes are critical to evaluate whether conditions are suitable for life and biosignature detection. Radar sounding is a powerful geophysical technique to probe the thermophysical and chemical properties of icy moons, like Enceladus, and to investigate the subsurface context for the exchange of material and energy between their subsurface oceans, ice shells, and plumes. To inform the scientific potential and instrument performance demands of such a radar-sounding investigation of Enceladus' ice shell, we adapt and extend previous radar attenuation analysis done for Europa to the configuration and conditions of Enceladus. We also discuss how attenuation (both as an obstacle for the detection of ice shell reflectors and as a signal itself) can help constrain the thermal, physical, and chemical configuration of Enceladus' ice shell and reveal the processes governing the moon's ocean/shell/plume system.

**Plain Language Summary** Enceladus, a tiny icy moon of Saturn, has been attracting attention since the discovery of its spectacular water jet activity. The jets, sampling the moon's hidden deep ocean, have revealed conditions favorable for the existence of life below the cold outer ice shell. Understanding the long-term persistence of the ocean, the jets, and their connection to the ice shell and ocean requires reliable knowledge of the shell's physical, thermal, and chemical properties. Ice penetrating radar is a powerful tool for studying ice shells in the planned missions to Jupiter's icy moons. In this paper, we expand and adapt the radar-based approach to Enceladus in light of the established constraints on the shell's structure and chemistry. We find that although the shell's chemical composition makes direct radar detection of the ice-ocean interface challenging, the shell's thermal structure enables constraining the thickness—and potentially chemistry—by future missions using echoes from water within the shell.

### 1. Introduction

Enceladus, a tiny moon of Saturn, is the subject of significant recent geophysical and astrobiological interest due mainly to the distinctive plumes emanating from its south-polar region (SPR). These plumes allowed the *Cassini* mission to sample the moon's interior and analyze the chemical composition. This analysis provided compelling evidence for direct contact between the silicate core and the internal ocean, and also for ongoing hydrothermal activity (Hsu et al., 2015; Schoenfeld et al., 2023; Waite et al., 2017). Consequently, Enceladus has been identified as a high-priority target for a search-for-life mission (Hendrix et al., 2019) and as the second highest priority new flagship-class mission for the upcoming decade (NASEM, 2022). Establishing constraints on the properties and structure of the ice shell and ocean is especially important in the context of life detection experiments and, more broadly, in the context of the moon's geophysical and geochemical evolution (Marusiak et al., 2021).

Current knowledge of Enceladus' structure relies on gravity (Iess et al., 2014) and topography (Tajeddine et al., 2017; Thomas et al., 2007) inversions, which are sensitive to the underlying model assumptions. For example, the assumption of hydrostatic equilibrium combined with Airy isostasy initially led to an overestimation of the ice shell thickness (Iess et al., 2014; McKinnon, 2015). Moreover, it was not possible to prove the existence of

© 2023. The Authors.

This is an open access article under the terms of the [Creative Commons Attribution-NonCommercial-NoDerivs License](https://creativecommons.org/licenses/by-nc-nd/4.0/), which permits use and distribution in any medium, provided the original work is properly cited, the use is non-commercial and no modifications or adaptations are made.

the (global) ocean without additional geodetic observations. Specifically, the detection and measurement of large amplitude libration provided the missing piece of evidence to support the existence of the global ocean (Thomas et al., 2016). The revised models of internal structure using combined topography-gravity-libration data predict a relatively thin ice shell with an average thickness of 14–26 km (Thomas et al., 2016; van Hoolst et al., 2016). This inversion also concluded that ice shell thickness varies from a few kilometers at the south pole to ~35 km in the equatorial region. Remarkably, even studies with different assumptions underpinning their interpretations (e.g., Beuthe et al., 2016; Čadek et al., 2016, 2019; Hemingway & Mittal, 2019) lead to similar ice-shell geometries. Based on these inversion models, the present-day image of Enceladus' structure involves a large (possibly unconsolidated and dissipative) core, a vast liquid water ocean underneath a relatively thin, most likely nonconvecting (Barr & McKinnon, 2007a) ice shell with substantial thickness variations and significant thinning at the south pole.

A large amount of data characterizing Enceladus' interior were collected thanks to jetting activity carrying the particles from the deep interior and emanating from an active fissure system (informally known as “tiger stripes”) concentrated near the south pole. The *Cassini* mission revealed the plume's composition and structure with water as the main constituent (see Postberg et al., 2018, for a review). Other abundant species include CO<sub>2</sub>, CH<sub>4</sub>, NH<sub>3</sub>, and H<sub>2</sub> (Waite et al., 2017). Compositional analysis of the E-ring fed by the plume also revealed salt-rich ice grains and silica nanoparticles (Hsu et al., 2015). Both the presence of molecular hydrogen and silica nanoparticles point to ongoing hydrothermal activity connected to the silicate-rich core. The conditions necessary to create nanoparticles are consistent with pH > 8.5 and temperature >90°C at the core-ocean interface; such conditions suggest a strong habitability potential (Higgins et al., 2021; McKay et al., 2018). The structure and high-temperature conditions in the interior are also important indicators of the past evolution, energy budget, and long-term sustainability of the ocean and hydrothermal activity (e.g., Schoenfeld et al., 2023; Soderlund et al., 2020). Consequently, providing improved estimates of the ice-shell thickness and its thermal state is of key importance.

On Earth, airborne ice-penetrating radar sounders have been long and successfully used to constrain the structure and subsurface conditions of terrestrial ice sheets (e.g., Dowdeswell & Evans, 2004; Schroeder et al., 2020). Recently, orbital radar instruments MARSIS (Picardi et al., 2005) and SHARAD (Seu et al., 2007) have successfully investigated Mars' polar caps (Phillips et al., 2008; Plaut et al., 2007) and ice-penetrating radar sounders will also be carried by the upcoming large missions to the icy moons—the RIME instrument (Bruzzone et al., 2015) onboard ESA's *JUICE* spacecraft and the REASON instrument (Blankenship et al., 2009; Scanlan et al., 2021) onboard NASA's *Europa Clipper*. The main goals of these instruments will be to search for the ocean interface and to study the distribution of shallow subsurface water as well as the thermophysical structure of the ice shell.

Although ice-penetrating radars are successful in sounding terrestrial ice sheets and Martian polar caps, one must keep in mind that they are only a few kilometers thick while the average thicknesses of the shells of Europa and Enceladus are estimated to be more than ~15 km (e.g., Čadek et al., 2019; Howell, 2021). Full shell radar penetration for Europa and Enceladus is therefore expected to be extremely challenging, but detectable radar echoes could be observed from reflective subsurface structures defined by dielectric contrasts (e.g., density/chemistry/phase interfaces, thermal/crystal structures; Dowdeswell & Evans, 2004). These echoes might constrain the shells' structures and, since radar signal attenuation is strongly modulated by both temperature and chemical composition, radar measurements could potentially also constrain these thermo-compositional characteristics.

While no authors have yet studied radar performance on Enceladus, several studies have investigated the potential for sounding Europa's ice shell. Initially, only cold conductive shells ≤10 km thick were predicted to allow ocean detection (Blankenship et al., 2009; Chyba et al., 1998; Moore, 2000). Later studies investigated penetration through a cold downwelling which would allow the detection of an ocean up to ~15 km deep (Di Paolo et al., 2014, 2017; Kalousová et al., 2017; McKinnon, 2005). However, the warmest (and therefore most attenuating) ice is nearest the ocean, so the numbers for “direct ocean detection” in this paragraph are conservative in this respect. Additionally, these studies are for generic radar link budgets, meaning that specific implementations and performance numbers for existing and future radar sounders can result in lower or higher penetration depths. Kalousová et al. (2017) showed that the two-way attenuation to the eutectic isotherm is ≤30 dB providing a specific robustly detectable (and thermally diagnostic) target for investigation of the ice shell's structure. Reflectivities of eutectic layers within Europa's ice shell were in detail studied by Culha et al. (2020).

The aim of this manuscript is to build on the work of Kalousová et al. (2017) and investigate the performance of a generic radar sounder at Enceladus. While considering the uncertainty in the shell's thermal regime and chemical composition, we focus on the possibility of directly detecting the ice-ocean interface and two endmember eutectic isotherms. The structure of this paper is as follows: In Section 2, we provide a brief overview of the attenuation and thermal models. Our results are described in Section 3 and discussed in Section 4. We conclude this study in Section 5, where we give the summary of our results and their implications for the potential performance of ice-penetrating radar in constraining the thickness, temperature, and chemistry of Enceladus' ice shell.

## 2. Methods

### 2.1. Radar Attenuation

The electromagnetic waves transmitted by radar on an orbiting spacecraft will be attenuated while propagating through a planetary ice shell and reflected from subsurface interfaces. Using the same approximations as in terrestrial polar ice sounding (e.g., MacGregor et al., 2007; Matsuoka et al., 2010), the power  $P_r(d)$  (returned from an interface at depth  $d$ ) measured by the orbiting radar can be approximated as (e.g., Di Paolo et al., 2017; Pettinelli et al., 2015) follows:

$$P_r(d) \simeq R(d)A_2(d)P_c, \quad (1)$$

with  $R(d)$  the interface reflectivity,  $A_2(d)$  the two-way attenuation along the propagation path, and  $P_c$  the corrected irradiated power which accounts for the effects of geometric spreading and birefringence, although the latter is negligible here (see also Kalousová et al., 2017, for more details). Because both the subsurface reflection coefficient and the attenuation depend on the physical properties within the ice shell, the data collected by the radar receiver can help constrain the properties and structure of the shell interior.

Within the range of HF and VHF frequencies used by radar sounders (Schroeder et al., 2020), the (one-way) attenuation  $A_1$  (in dB/km) in ice is proportional to the electrical conductivity  $\sigma$  (in  $\mu\text{S m}^{-1}$ ) (e.g., Matsuoka et al., 2012):

$$A_1 \approx 0.914 \sigma. \quad (2)$$

The electrical conductivity of ice in the absence of brine depends on the concentration of conductivity-enhancing impurities (e.g., acid, chloride, and ammonium) and temperature and can be evaluated as (see e.g., Corr et al., 1993) follows:

$$\sigma = \sum_i \sigma_i^0 C_i \exp \left[ -\frac{E_i}{k_B} \left( \frac{1}{T} - \frac{1}{T_r} \right) \right], \quad (3)$$

with  $i = 0$  indicating pure ice and  $i > 0$  the added conductivity-enhancing impurities. In Equation 3,  $\sigma_0^0$  is the pure ice conductivity and  $\sigma_i^0$  are the molar conductivities of the impurities at the reference temperature  $T_r = 251$  K,  $C_i$  are the molar concentrations (with  $C_0 = 1$ ),  $E_i$  are the activation energies,  $T$  is the (absolute) ice temperature, and  $k_B$  is the Boltzmann constant. All parameters are listed in Table 1.

Unlike Europa, there are constraints on the composition of Enceladus' ocean chemistry from the plume material sampled by *Cassini* (e.g., Glein et al., 2018). Assuming that the composition of the plume material is representative of the ocean, this suggests that the ocean is dominated by chloride and carbonate salts and that ammonia/ammonium ( $\text{NH}_3/\text{NH}_4^+$ ) and silica are also present but at lower concentrations (Fox-Powell & Cousins, 2021; Glein et al., 2018). Of these species, only chloride and ammonium can contribute to the electrical conductivity of ice modeled in Equation (3). Plume material implies a lower bound ocean chlorinity of  $\sim 50,000$   $\mu\text{M}$  and an upper bound of  $\sim 200,000$   $\mu\text{M}$  (Glein et al., 2018), although the bulk ocean chlorinity could be significantly higher if the plumes are sourced from a low salinity water layer beneath the polar ice shell (Kang et al., 2022; Lobo et al., 2021; Zeng & Jansen, 2021). Estimates of  $\text{NH}_3$  and  $\text{NH}_4^+$  concentration, which assume fractional distillation of gases occurs within the plume vents, suggest the value could be as low as  $\sim 1$   $\mu\text{M}$ ; however, we follow Fox-Powell and Cousins (2021) and adopt their "mid-range" value of 1,000  $\mu\text{M}$ . Assuming that the ice shell forms through equilibrium freezing of sodium chloride (NaCl) solution, 0.278% of the chloride will be incorporated into the ice (Gross et al., 1977). This yields a lower bound ice chlorinity of 130  $\mu\text{M}$  and an upper bound of 556  $\mu\text{M}$ , where the upper bound exceeds the 300  $\mu\text{M}$  solubility limit for chloride in ice (Moore et al., 1994;

**Table 1**  
*Model Parameters*

Symbol	Physical property	Value	Unit
$T_r$	Conductivity reference temperature <sup>a</sup>	251	K
$T_{NH_4Cl}^e$	NH <sub>4</sub> Cl eutectic temperature <sup>b</sup>	257.79	K
$T_{NH_3}^e$	NH <sub>3</sub> eutectic temperature <sup>b</sup>	175.45	K
$k_B$	Boltzmann constant	$8.6173 \times 10^{-5}$	eV K <sup>-1</sup>
$\sigma_0^0$	Electrical conductivity of pure ice <sup>a</sup>	7.2	$\mu\text{S m}^{-1}$
$C_0$	Auxiliary constant	1	–
$E_0$	Activation energy of pure ice <sup>a</sup>	0.55	eV
$\sigma_0^1$	Molar electrical conductivity of Cl <sup>a</sup>	0.43	$\text{S m}^{-1} \text{M}^{-1}$
$C_1$	Radar effective molar concentration of Cl <sup>c</sup>	0, 10, 100, 200, 300	$\mu\text{M}$
$E_1$	Activation energy of Cl <sup>a</sup>	0.19	eV
$k_0$	Thermal conductivity parameter <sup>d</sup>	651	$\text{W m}^{-1}$

<sup>a</sup>MacGregor et al., 2007. <sup>b</sup>Marion et al., 2012. <sup>c</sup>Stillman et al., 2013. <sup>d</sup>Petrenko and Whitworth 2002.

Stillman et al., 2013). When ammonium is present, both chloride and ammonium are incorporated into the ice at a higher efficiency of 1.37% (Gross et al., 1977). However, because the concentration of ammonium is estimated to 1,000  $\mu\text{M}$ , this translates to approximately 10  $\mu\text{M}$  ammonium chloride (NH<sub>4</sub>Cl) in the ice. Given that the molar conductivities of Cl<sup>-</sup> and NH<sub>4</sub><sup>+</sup> are of the same order (MacGregor et al., 2007), we neglect the contribution of ammonium and consider ice shell chlorinities of 100, 200, and 300  $\mu\text{M}$ . We also consider pure ice (0  $\mu\text{M}$ ) and a chlorinity of 10  $\mu\text{M}$  to represent ice shells that are more transparent to radar.

The two-way attenuation  $A_2(d)$  experienced by the signal during its path to and from a reflecting interface at depth  $d$  is calculated as twice the path integral of  $A_1$  from the surface ( $d = 0$ ) to a depth  $d$ . In the simplest case, that is, for a vertical ray, it reads as follows:

$$A_2(d) = 2 \int_0^d A_1(s) ds, \quad (4)$$

where  $A_1(s)$  denotes the one-way attenuation at depth  $s$ .

We calculate the two-way attenuation to the ice-ocean interface as well as to two possible eutectic interfaces, where we define the eutectic interface as the depth within the ice shell where liquid water becomes thermodynamically stable (i.e., where the temperature equals the eutectic temperature). Recall that it is the composition—and not concentration—of impurities that governs the eutectic temperature (Wolfenbarger, Fox-Powell et al., 2022). Therefore, although NaCl (~252 K) is more abundant, we choose NH<sub>3</sub> (175.45 K) and NH<sub>4</sub>Cl (257.79 K) to define our eutectic interfaces (Marion et al., 2012). This decision enables us to represent upper and low end-members of possible eutectic temperatures while simultaneously considering the effect of oceanic pH, which will govern whether ammoniac nitrogen is in the form of ammonium or ammonia (Fox-Powell & Cousins, 2021).

Although detection of the ice-ocean interface would enable direct measurement of the total ice shell thickness, detection of liquid water within the shell establishes constraints on the minimum ice shell thickness or allows one to infer the shell thickness indirectly (see the discussion in Section 4). Because the eutectic interface likely represents the first ice-water interface that the radar signal encounters as it traverses the ice shell, the two-way attenuation to the eutectic interface will always be lower than the two-way attenuation to the ice-ocean interface. As a result, echoes from a eutectic interface could be detected by radar sounders with link budgets that exceed the two-way attenuation by more than the effective reflectivity of the eutectic interface (Culha et al., 2020). This detection of a eutectic interface could constrain the local thermal profile if the ice shell composition is known (e.g., from spectrometer data) or constrain the composition if the local thermal profile and/or state is known (e.g., from thermal imager or radiometer data). In either case, detectable eutectic interfaces would likely locally shadow any deeper interfaces including the ice-ocean interface (as observed beneath near-surface water bodies in Greenland (Culberg et al., 2022)).

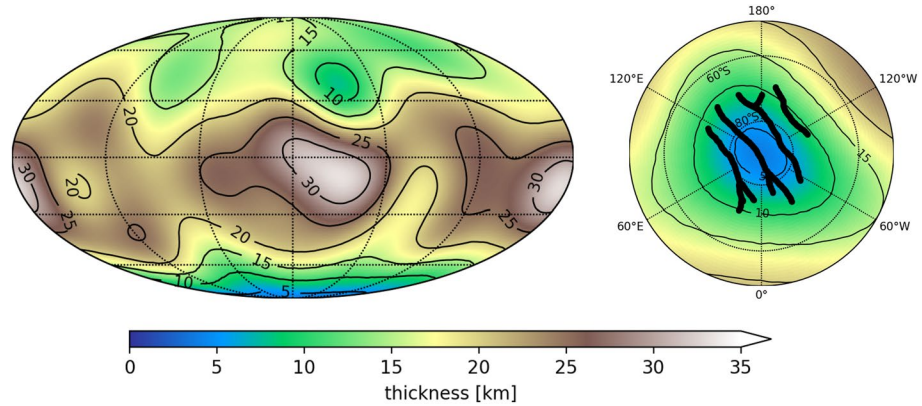


**Figure 1.** Shell thickness model based on Tajeddine et al. (2017) and Čadek et al. (2019); a global view in Mollweide projection (left) and a zoom of the south-polar region in stereographic projection (for colatitudes 140°–180°) (right).

## 2.2. Thermal Structure of Enceladus' Shell

### 2.2.1. 3D Model

The synthetic temperature structure of Enceladus' ice shell, which is used as an input in this study, is based on the model from Souček et al. (2019). The authors developed a 3D finite-element model of Enceladus' ice shell which involves realistic variations of the shell thickness and shape based on Tajeddine et al. (2017) and Čadek et al. (2019), see Figure 1. The model also takes into account the local effects associated with tiger stripes (see Figure 1 right).

Ice is described by a viscoelastic Maxwell rheology with temperature-dependent viscosity. The viscosity is described by a reference value at the melting point, which depends on the properties of the shell such as the ice grain size. In this study, we consider a model from Souček et al. (2019) with this reference value taken as  $3 \times 10^{14}$  Pa s—a value shown in Čadek et al. (2019) to be the lowermost possible that is consistent with a dynamic steady-state shape of Enceladus. The model computes the thermo-mechanical periodic steady state of the ice shell resulting from periodic forcing induced by the varying tidal potential. Assuming a purely conductive heat transfer with the thermal conductivity given by Petrenko and Whitworth (2002),

$$k(T) = \frac{k_0}{T}, \quad \text{with} \quad k_0 = 651 \text{ W m}^{-1}, \quad (5)$$

the model solves for the temperature structure within the ice shell self-consistently with its mechanical state, that is, by incorporating the mechanical dissipation due to tidal deformation as the heat source and, at the same time, considering the temperature dependence of viscosity through the Arrhenius formula. An effective surface temperature of 59 K corresponding to the equilibrium temperature (Beuthe, 2018; de Pater & Lissauer, 2001) and a melting point temperature of 273.15 K are prescribed at the surface and ice-ocean interface, respectively. The model employs a simplified description of the fault system as narrow zones of negligible mechanical resistance passing through the whole shell, approximating thus the faults as frictionless and hydrostatically flooded by water from the internal ocean. As a consequence of this simplification, the model does not involve realistic estimates of mechanical dissipation due to friction at the faults (estimated in Pleiner Sládková et al. (2021) to be  $\leq 1$  GW). Instead, the temperature inside the fault zone is prescribed to be at the melting point. For further details on the model and on the numerical implementation in FEniCS (Alnaes et al., 2015; Logg et al., 2012) finite-element open source library, we refer to Souček et al. (2019).

### 2.2.2. Analytical 1D Model

For better insight, we also consider a simplified 1D model of the thermal structure of the shell. This model is obtained analytically by solving the stationary heat-conduction problem based on the thermal conductivity given by Equation 5, on a spherical shell with uniform thickness  $D$  and outer and inner radii  $R_{\text{top}} = 252$  km and  $R_{\text{bot}} = R_{\text{top}} - D$ , and with the temperature boundary conditions as in the 3D model:

$$\frac{1}{r^2} \frac{d}{dr} \left( r^2 \frac{k_0}{T} \frac{dT}{dr} \right) = 0, \quad r \in (R_{\text{bot}}, R_{\text{top}}), \quad (6)$$

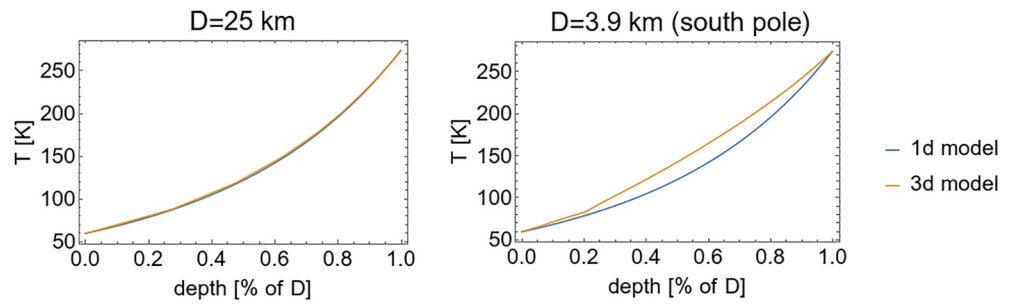


**Figure 2.** A comparison of the vertical temperature profiles from the 3D model and the analytical 1D model. Left: A point representative of average shell thickness  $D \doteq 25$  km ( $\theta = 128^\circ$ ,  $\phi = 249^\circ$ ). Right: south pole with  $D \doteq 3.9$  km.

$$T = T_{\text{top}} = 59 \text{ K at } r = R_{\text{top}}, \quad (7)$$

$$T = T_{\text{bot}} = 273.15 \text{ K at } r = R_{\text{bot}}. \quad (8)$$

The solution to this problem (found most easily by reformulating this problem in terms of a new unknown  $\ln(T)$ ), reads

$$T(r) = T_{\text{bot}} e^{Z R_{\text{top}}(r - R_{\text{bot}})/r} \quad \text{where} \quad Z = \frac{\ln T_{\text{top}} - \ln T_{\text{bot}}}{D}. \quad (9)$$

In regions with small dissipative heating and local shell thickness  $D$ , this analytical solution corresponds well to the temperature profile obtained from the 3D model. The correspondence between the 1D and 3D temperature solutions deteriorates in locations with enhanced dissipation or other 3D effects, such as the SPR, see Figure 2, where a comparison at two different locations is shown—a point representative of the mean shell thickness and the south pole.

### 3. Results

In Figure 3, we plot the two-way attenuation  $A_2$  based on the 3D temperature field for the ice-ocean interface considering five chlorinity values  $C = 0\text{--}300 \mu\text{M}$ . As an upper bound for the radar detectability, we consider a threshold value of  $A_2^{\text{max}} = 100$  dB. This represents a detection threshold comparable to that used by Kalousová et al. (2017) to represent the potential performance of an ice-penetrating radar instrument like REASON on the upcoming NASA *Europa Clipper* mission (Blankenship et al., 2009; West et al., 2017). The attenuation values correlate well with the thickness variations, where the attenuation maxima and minima coincide with the shell thickness maxima and minima, respectively (see Figure 1). In the south-polar region, this simple relation is disturbed by the presence of faults, which serve in the model as heat sources with a prescribed temperature equal to the melting point. Consequently, this leads to an increase in temperature and thus also attenuation values in the faults' vicinity. This effect is superposed by the long-wavelength attenuation reduction due to shell thinning, which results in a relatively complex attenuation pattern in the SPR. In order to suppress the effect of perhaps questionable temperature conditions specified within the fault zones in our model, we do not show any data there, plotting black lines at the positions of the fault zones.

The results shown in Figure 3 indicate that even with the lower-end chlorinity estimate of  $C = 100 \mu\text{M}$ , the ice-ocean interface is undetectable except for the thin south-polar region. In contrast, most of the interface would be detectable globally for chlorinity levels  $C \leq 10 \mu\text{M}$ .

This conclusion is further supported in Figure 4, where we plot the fraction of the shell thickness penetrable by the radar depending on the considered threshold attenuation value  $A_2^{\text{max}}$ , while considering various chlorinities. Here, we employ the 1D analytical temperature profile (9) considering three values of the local shell thickness:  $D = 25$  km,  $D = 5$  km, and  $D = 30$  km, representative of the mean shell thickness, the south-polar region, and the equatorial region, respectively. We can see that for  $D = 25$  km and  $A_2^{\text{max}} = 100$  dB, the shell is fully penetrable by the radar only for  $C \leq 10 \mu\text{M}$ , while for  $D = 30$  km, this holds only for pure ice ( $C = 0 \mu\text{M}$ ). On the other hand, thin ice with  $D = 5$  km and chlorinity equal to  $C = 100 \mu\text{M}$  (and lower) admits full penetration. This implies that,

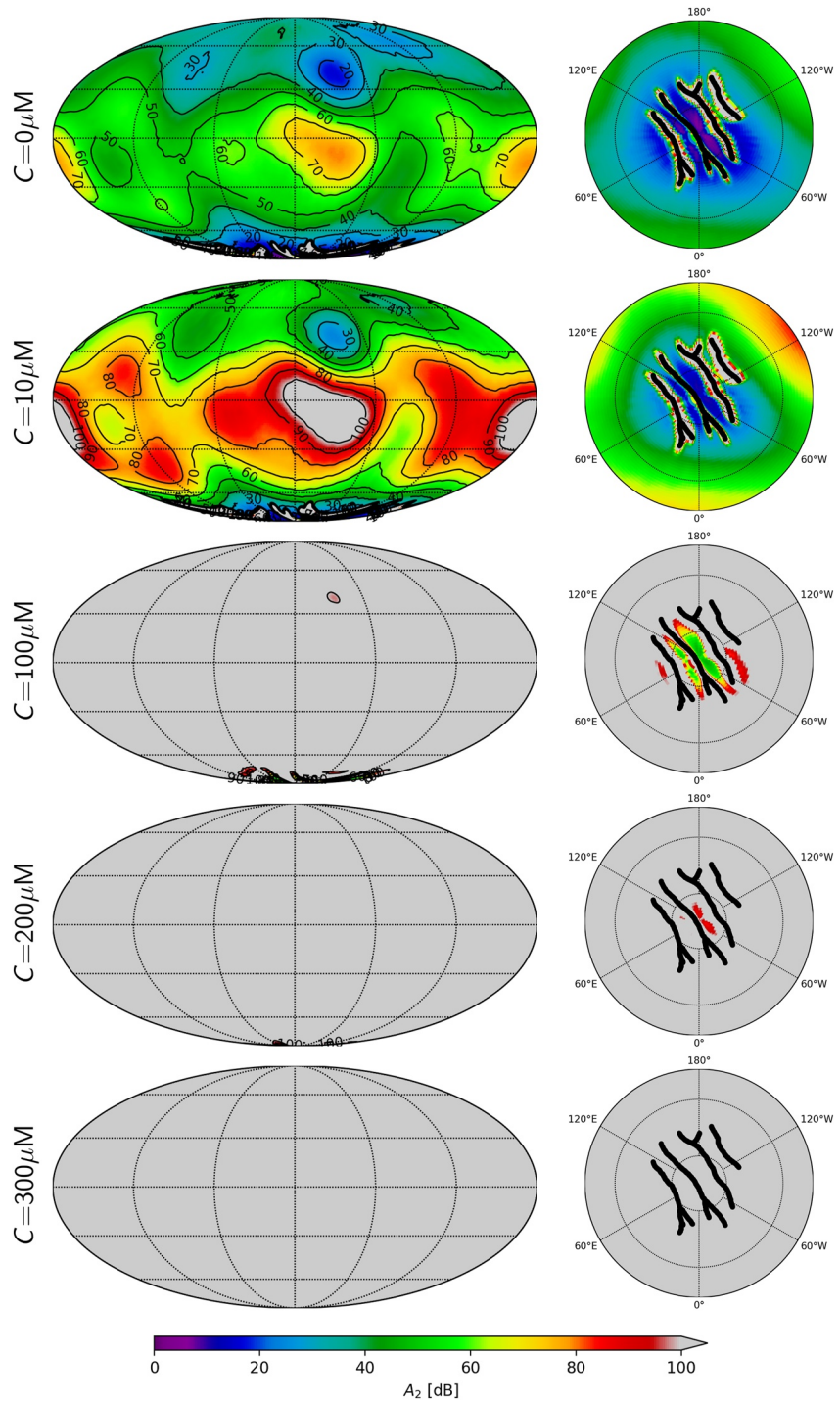


**Figure 3.** Two-way attenuation  $A_2$  for the ice-ocean interface with chlorinities  $C = 0\text{--}300\ \mu\text{M}$ . Views and projections as in Figure 1.

in the south-polar region, the ice-ocean interface could be potentially detectable by a radar instrument with such (100 dB) dynamic range.

Figure 4 also demonstrates that the composition-related uncertainty in attenuation becomes very large for reflectors located in the deep, warm, high-loss part of the shell. For instance, at a location with a shell thickness of 25 km and a reflective interface located 1.25 km above the ice-ocean interface (i.e., the penetration depth of 95% of the thickness), the two-way attenuation to this reflector for pure ice is about 7.5 dB, for  $C = 10\ \mu\text{M}$  about

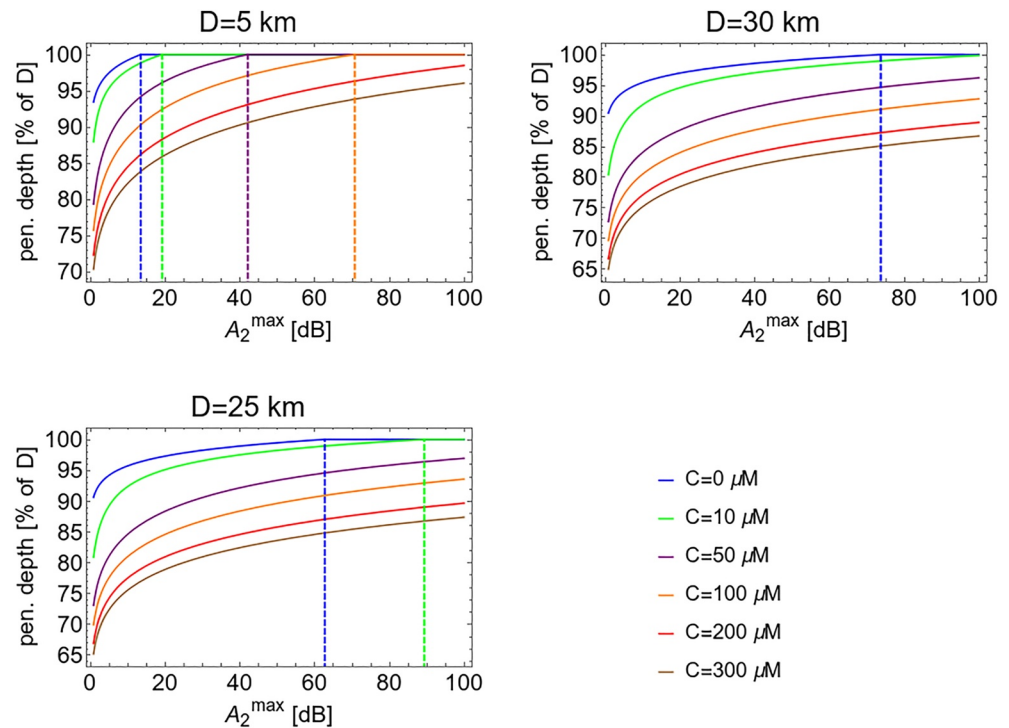


**Figure 4.** Fraction of shell thickness penetrated by the radar (in percent) as a function of  $A_2^{\max}$  for different composition models. The three panels correspond to the different local thicknesses of the shell. Top left:  $D = 5$  km, shell thickness characteristic of the south-polar region, Top right:  $D = 30$  km, shell thickness characteristic of the equatorial region, Bottom left:  $D = 25$  km, mean shell thickness. The vertical dashed lines correspond to the minimum values of  $A_2^{\max}$  threshold, for which the whole-shell penetration is reached.

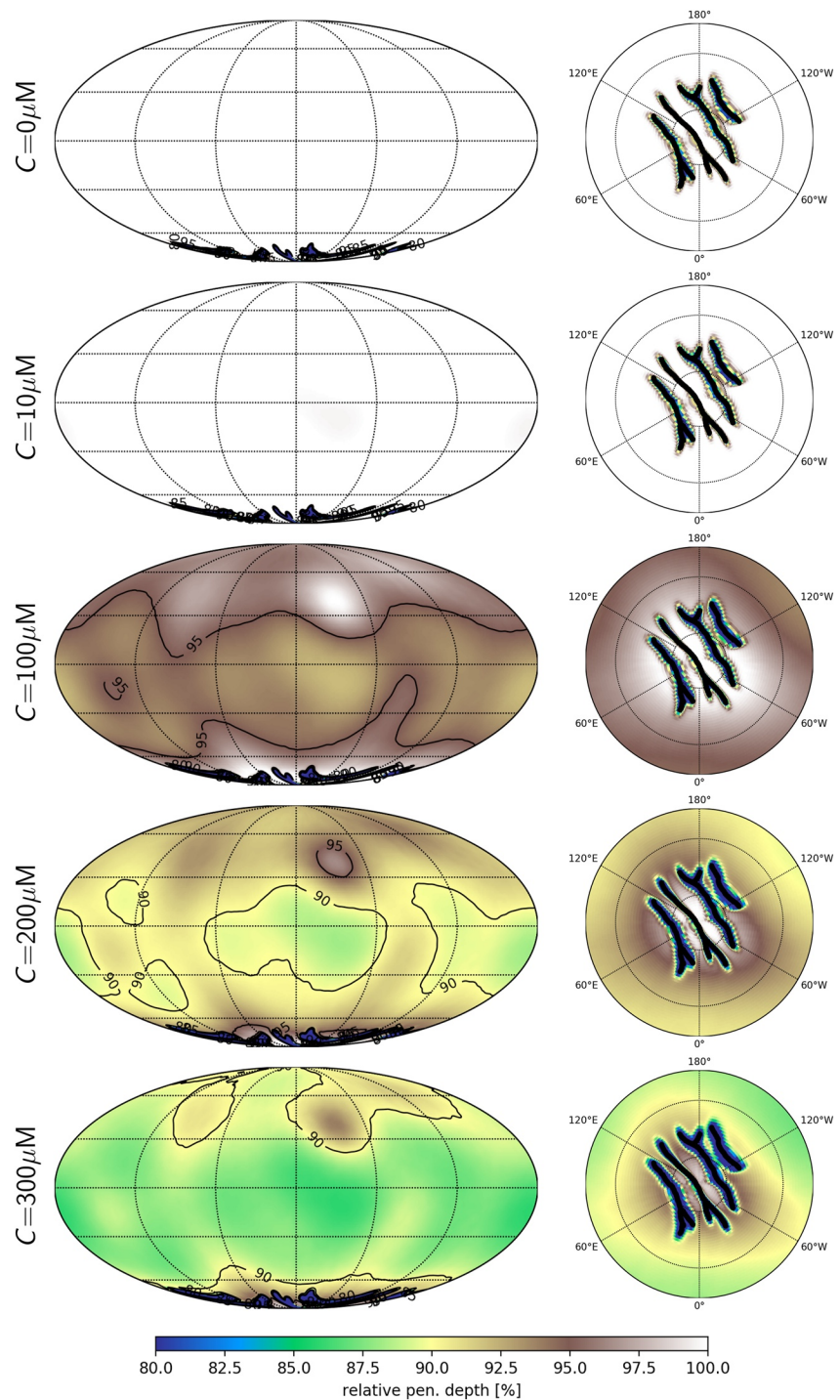
20 dB, for  $C = 50 \mu\text{M}$  about 68 dB, and for  $C = 100 \mu\text{M}$  already 129 dB. This also implies that a potential knowledge of attenuation to a well-localized deep reflector could be used to strongly constrain the shell's chemistry, see also discussion in Section 4. Note that for shallower reflectors, the chemistry-related uncertainty in attenuation becomes smaller. So while being easier to detect, these shallow reflectors would potentially pose weaker constraints on the shell's chemistry than the deeper ones.

Figure 5 expands the conclusions inferred from the 1D model to the 3D case. It shows the relative penetration depths (as a fraction of the local shell thickness shown in Figure 1) for the value  $A_2^{\max} = 100$  dB based on the 3D temperature field and for different chlorinities  $C = 0$ – $300 \mu\text{M}$ . This figure refines the conclusions based on the 1D analytical model with the spatial variations expressing the 3D structural effects and the effect of mechanical heating (not considered in the 1D model). In accordance with the previous two figures, we observe that detection of the ice-ocean interface might be possible for a chlorinity of  $C = 100 \mu\text{M}$  (and lower) in the thinnest south-polar part of the shell, while the global detection of the ice-ocean interface would require a chlorinity  $C \leq 10 \mu\text{M}$ .

In Figures 6 and 7, we plot the two-way attenuation  $A_2$  at depth levels corresponding to the eutectics of  $\text{NH}_4\text{Cl}$  and  $\text{NH}_3$ , respectively, considered here as representative candidates for reflective interfaces within the shell. Both eutectics are defined as isothermal surfaces corresponding to the eutectic temperatures  $T_{\text{NH}_4\text{Cl}}^e = 257.79$  K and  $T_{\text{NH}_3}^e = 175.45$  K, respectively (Marion et al., 2012).

Considering the same detection threshold as before, that is,  $A_2^{\max} = 100$  dB, the  $\text{NH}_4\text{Cl}$  eutectic, shown in Figure 6, appears to be detectable in the SPR even for the highest considered chlorinity  $C = 300 \mu\text{M}$ , even though in this case only locally in the vicinity of the south pole. For the intermediate value  $C = 200 \mu\text{M}$ , a slightly larger portion of the south-polar eutectic surface is detectable, while for  $C = 100 \mu\text{M}$ , a relatively large portion of SPR, as well as a patch in the northern hemisphere correlating with the local thickness minima are visible. Finally, for chlorinities lower than  $10 \mu\text{M}$ , most of the eutectic interface would be detectable by radar.





**Figure 5.** Relative penetration depth for attenuation threshold  $A_2^{\max} = 100$  dB. Views and projections as in Figure 1.

The level of  $A_2$  attenuation to the  $\text{NH}_3$  eutectic interface, shown in Figure 7, is almost an order of magnitude lower than that to the  $\text{NH}_4\text{Cl}$  eutectic due to its significantly lower temperature. Consequently, the corresponding value of  $A_2$  does not exceed 20 dB even for the highest considered chlorinity  $C = 300 \mu\text{M}$  (note the different color scales in Figures 6 and 7). The  $\text{NH}_3$  eutectic interface should thus be well detectable irrespective of the ice shell's chlorinity.

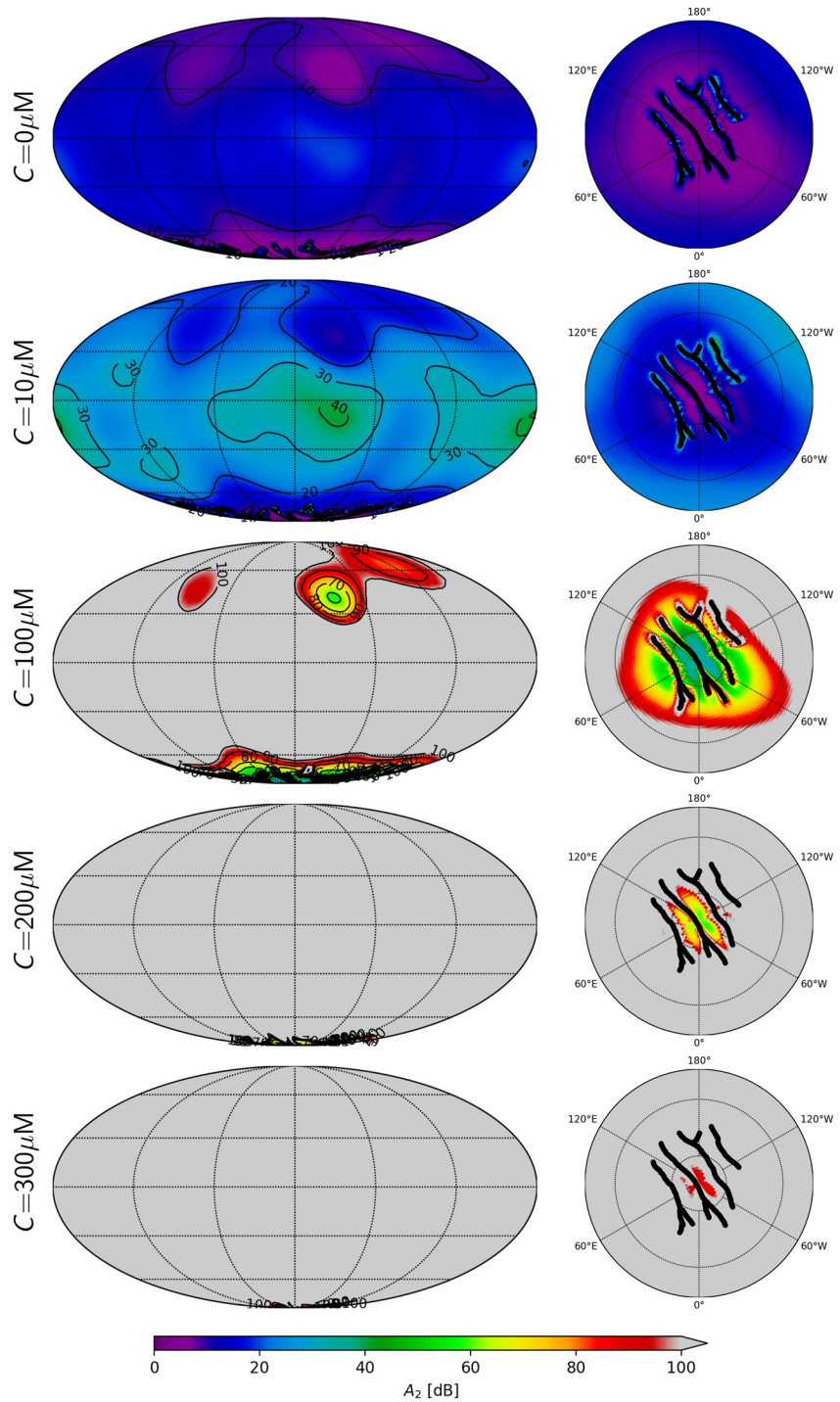


**Figure 6.** Two-way attenuation  $A_2$  to the  $\text{NH}_4\text{Cl}$  eutectic. Views and projections as in Figure 1.

#### 4. Discussion

Our results indicate that detection of any of the three considered reflective interfaces, that is, the ice-ocean interface or either of the two eutectics ( $\text{NH}_4\text{Cl}$  or  $\text{NH}_3$ ), could be used to constrain the ice shell's structure. While this is clear for the most challenging (and thus the least probable) direct detection of the ice-ocean interface, it is also true for both of the eutectic isotherms we modeled. Indeed, based on our results, there appears to be a direct correlation between the eutectic depths and the shell thickness. However, this correlation relies strongly

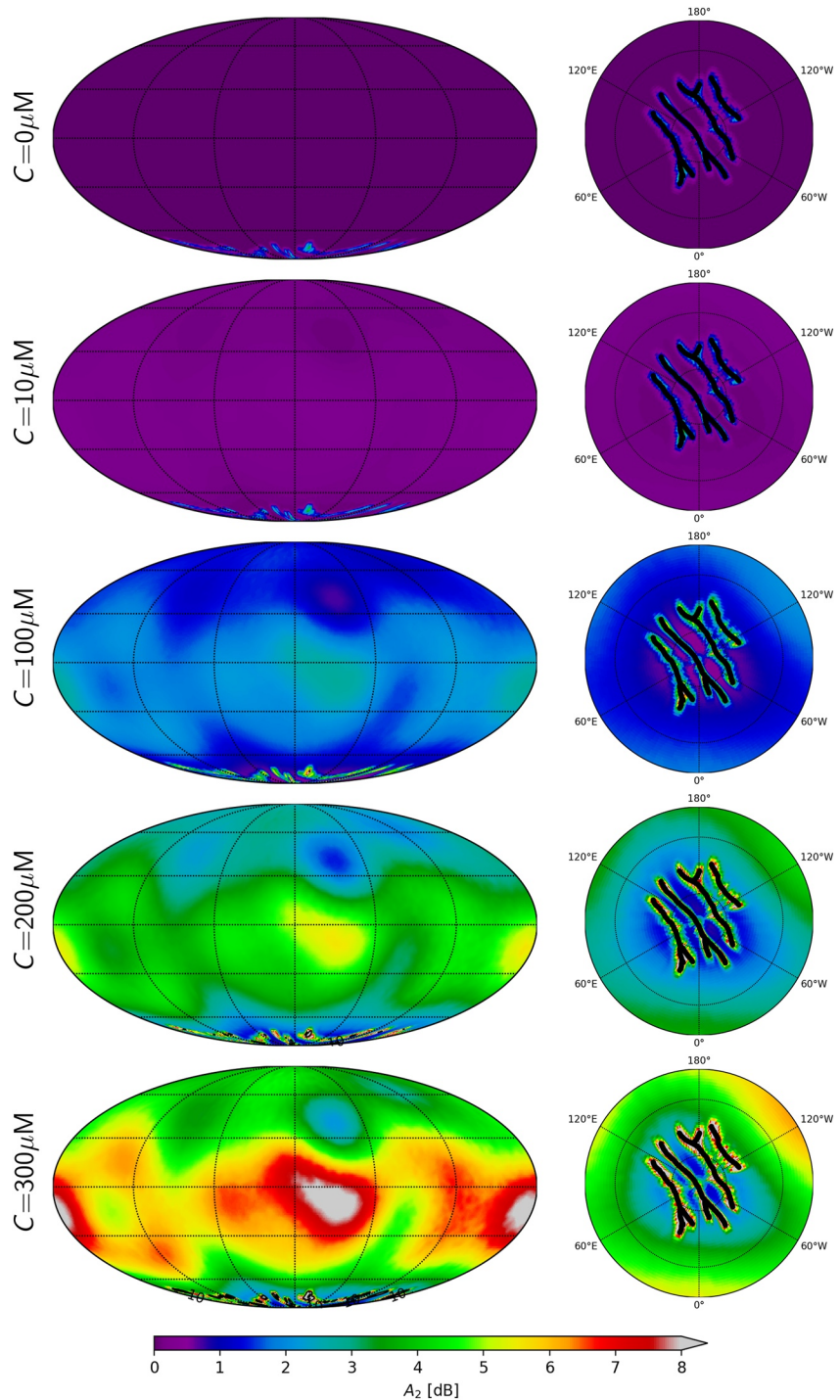


**Figure 7.** Two-way attenuation  $A_2$  to the  $\text{NH}_3$  eutectic. Views and projections as in Figure 1.

on the assumption that the heat transfer regime within the shell is purely conductive. This is presently a widely accepted view since the (local) Rayleigh number is almost certainly below the critical one due to low gravity, small shell thickness, and a relatively high estimate of the basal ice viscosity. Existing thermal convection studies (Barr & McKinnon, 2007a; Mitri & Showman, 2008) conclude that only a viscosity comparable to or lower than  $10^{13}$  Pa s can trigger convection in Enceladus' ice shell. This holds for the shell thickness at the equator (35–40 km) and, for thinner shells, the conditions would be even more unfavorable for convection. Such low ice viscosity at the base of the shell is, however, inconsistent with the long-term stability of the large ice shell

thickness variations as predicted today (Čadek et al., 2019). Additionally, such low viscosity values correspond to grain sizes lower than 0.1 mm, and maintaining such fine grain structure through boundary pinning would probably require a significant content of impurities (Barr & McKinnon, 2007a, 2007b; Běhounková et al., 2013). Additionally, Barr (2008) suggested that convection may be facilitated as a consequence of the finite strength of ice; however, only for model values lower than the measured yield stress. All these arguments support the premise of a conductive regime within the shell of Enceladus. If surprisingly, thermal convection takes place in Enceladus' ice shell, its temperature structure and therefore the estimates of attenuation and penetration depths would be altered significantly. Quantitative insight into the effect of convection within the shell would require a dedicated numerical study, similarly as in Kalousová et al. (2017) for Europa, which is out of the scope of this paper. Let us note, however, that the conclusions of this study would most likely hold in the SPR, where only a few-kilometer thick crust should remain in a conductive state.

Adopting the assumption of a purely conductive regime within the shell, our finite-element calculations interestingly indicate that the thermal structure of a 3D shell with realistic shape variations, with Maxwellian rheology and with the inclusion of dissipative heating, can be reasonably well approximated by a (local) 1D analytical profile. This holds except for the south-polar region, where the fault system known as tiger stripes makes the temperature regime more complex. Consequently, for most of the shell, radar sounding measurements from the reflective eutectic interfaces within the shell would provide a unique structure-sampling tool. In particular, the detection of some or both of the discussed eutectic interfaces could be used to constrain the shell thickness as follows: The 1D analytical model of the shell's thermal structure (9) can be inverted for the local shell thickness  $D$  if applied to the prescribed eutectic  $T^{\text{eut}}$ , that is, considering the relationship  $T^{\text{eut}} = T(R^{\text{top}} - d)$  where  $d$  is the (measured) depth of the eutectic and with the function  $T(\cdot)$  on the right-hand side given by Equation (9). This way, detecting the depth of a known (eutectic) isotherm would allow the determination of the local shell thickness. In this case, the detection (and identification) of echoes from the eutectic at a given depth is all that is required to map the ice shell thickness. The significantly lower attenuation to the eutectic isotherms (Figures 6 and 7) compared to the ice-ocean interface (Figure 3) has the potential to dramatically relax requirements for and increase the robustness of ice-shell thickness estimates from radar sounding.

In the detection-only analysis approach described above, many potentially complicating factors can be comfortably neglected. This includes carefully constraining, calibrating, or knowing the radar beam pattern, the absolute radiometric calibration of the radar, two-way rough surface transmission losses (Schroeder et al., 2016), volume scattering losses (Aglyamov et al., 2017), and the effective reflectivity of the eutectic interface (Culha et al., 2020). However, if these challenging calibration, system, and analysis requirements could be met, the inversion for thickness and (1D) temperature profile described above can be expanded to also constrain the impurity profile as follows: If the radar instrument would be able to measure the (relative) power of the received signal, from Equation 1, we see that when given a model for reflectivity  $R$ , it would provide the value of associated two-way attenuation  $A_2(d)$  to the given eutectic. This value of  $A_2(d)$  is determined by the depth integral of  $A_1$  via Equation 4, where  $A_1$  depends on temperature and composition through Equations 2 and 3. With the local temperature profile known, given by Equation 9 with  $D$  determined in the first step, the  $A_2(d)$  value provides a constraint on the chemical composition of the shell. Considering only chlorine as the conductivity-enhancing impurity, its amount (constant or arbitrary one-parametric depth profile) could thus be uniquely determined in the second step of the inversion. As shown in Figure 4, the compositional sensitivity of attenuation is largest for deep reflectors located in the warm high-loss portion of the shell (such as the  $\text{NH}_4\text{Cl}$  eutectic or the ice-ocean interface itself). Consequently, while the detection-only localization of shallow reflectors (such as the  $\text{NH}_3$  eutectic) would suffice to constrain the shell thickness, a robust constraint on the shell's chemistry may require calibration and careful quantitative analysis of the echos from deep reflectors.

In our study, we considered a homogeneous boundary condition for the surface temperature  $T_s = 59$  K (consistently with the underlying simulations in Souček et al. (2019)), neglecting its latitudinal dependence (Nadeau & McGehee, 2017; Ojakangas & Stevenson, 1989; Weller et al., 2019). In order to quantify the effect of this simplification, we used the analytical 1D model, described in Section 2.2, considering the surface temperature range 48–63 K between the poles and the equator (Weller et al., 2019). We have computed the penetration depths as in Figure 4, using the values  $T_s = 48$  K for  $d = 5$  km (representing the south pole) and  $T_s = 63$  K for  $d = 30$  km (representing the equator). We found that the surface temperature effect is more pronounced at the pole where the

ice becomes easier to penetrate than in the equatorial area. In both cases, the penetration depths change by less than 5%. We have thus confirmed that the detectability of the three considered interfaces and its sensitivity to the shell's chlorinity remain unaffected by the simplified surface temperature parameterization.

The temperature field from the model by Souček et al. (2019) represents a quasi-steady state compatible with the tidal deformation and associated dissipation of a Maxwell viscoelastic body. Alternatively, an empirical Andrade viscoelastic model has been proposed for the tidal response of planetary ices (Castillo-Rogez et al., 2011). Using Andrade rheology instead of the Maxwell model might result in slightly enhanced dissipation, but our estimates based on the simplified parameterization of Andrade rheology in Souček et al. (2019) suggest that effects on the temperature field would be insignificant. At the same time, we have shown that, with the exception of the south-polar region, the effect of tidal heating itself is rather negligible and the temperature field could be well approximated locally by 1D analytical profiles without any heat sources. This suggests that our results are insensitive to the choice of ice rheology.

For all calculations, we considered a simple model of the electrical conductivity-enhancing chemical composition of the shell. In particular, we took into account only one such agent, chloride, for which we considered constant concentration (chlorinity) throughout the shell. Although neglecting the role of ammonium in governing radar attenuation is valid for the concentration assumed here, if the true concentration of ammonium significantly exceeds this estimate, it can no longer be neglected. Considering a constant ice chlorinity is also likely a good assumption, given that models of ice shell growth suggest the efficiency of salt entrainment is relatively uniform for most of the shell (Buffo et al., 2020; Vance et al., 2021; Wolfenbarger, Buffo, et al., 2022). Estimates of ice shell chlorinity could be greatly improved by dedicated experimental studies specifically focused on chloride entrainment in the ice lattice, particularly for multi-ion solutions containing ammonia/ammonium, sodium, and chloride. One limitation of the attenuation model implemented here is that it does not consider signal attenuation caused by brine pockets within the ice shell. For detection of a eutectic interface, neglecting this mechanism of signal attenuation is valid since brine is not thermodynamically stable above the eutectic interface; however, future work should consider this to develop improved estimates of radar signal attenuation to the ice-ocean interface.

## 5. Conclusions

In this study, we investigated the two-way radar attenuation to three potentially detectable reflective interfaces within the outer ice layer of Saturn's moon Enceladus: the ice-ocean interface and interfaces corresponding to the  $\text{NH}_4\text{Cl}$  and  $\text{NH}_3$  eutectics. We considered a realistic shellshape model based on recent topography and gravity inversions and a purely conductive temperature field consistent with the periodic steady-state tidal deformation of the shell described by a Maxwell viscoelastic model. Considering a range of compositions in terms of ice chlorinity, we have shown that the ice-ocean interface is globally detectable (for attenuation threshold of 100 dB) only for low levels of chlorinity of  $C \leq 10 \mu\text{M}$ . In the thin south-polar region, the ice-ocean interface may be detectable for chlorinities up to  $C \leq 100 \mu\text{M}$ . However, in this region, radar signal interpretation will probably be complicated due to structural complexities in the tiger stripe fault system, while the polar radar measurement itself is challenging on its own due to the instability of Enceladus' polar satellite orbit (Ermakov et al., 2021).

Concerning the  $\text{NH}_4\text{Cl}$  eutectic, the situation is analogous to the ice-ocean interface because the corresponding temperature is relatively close to the ice melting point. Consequently, the detection of reflective boundaries associated with this eutectic point is also mainly limited to the thickness minima in the south-polar region and potentially also in the northern hemisphere but only for ice chlorinities  $\leq 100 \mu\text{M}$ .

The situation is very different for the  $\text{NH}_3$  eutectic, which our model suggests should be globally detectable for chlorinities up to  $300 \mu\text{M}$ . Assuming a purely conductive heat transfer regime within the shell, attenuation to this eutectic correlates well with the shell thickness. Consequently, detection of the  $\text{NH}_3$  eutectic depth and knowledge of the associated attenuation could be used to infer both the local shell thickness and potentially constrain the ice chlorinity as well. While acquiring attenuation to the eutectic would have to be accompanied by precise evaluation of the radar signal power losses, detecting the eutectic depth is more straightforward. Despite the fact that direct global detection of the ice-ocean interface would place challenging requirements on any proposed Enceladus radar sounder, our study has confirmed a great potential of detecting the eutectic interface for mapping the ice shell structure, and possibly also for constraining its chemical composition.

## Data Availability Statement

All data for producing the figures are available in Souček et al. (2022).

## Acknowledgments

We thank B.H. Hills and one anonymous reviewer for their remarks and suggestions that helped to improve the clarity of the manuscript. This research was supported by the Czech Science Foundation through project No. 22-20388S (O.S., M.B., K.K.). A portion of this research was carried out at the Jet Propulsion Laboratory, California Institute of Technology, under a contract with the National Aeronautics and Space Administration (80NM0018D0004) and partially supported by the NASA Europa Clipper project.

## References

- Aglyamov, Y., Schroeder, D. M., & Vance, S. D. (2017). Bright prospects for radar detection of Europa's ocean. *Icarus*, *281*, 334–337. <https://doi.org/10.1016/j.icarus.2016.08.014>
- Alnaes, M. S., Blechta, J., Hake, J., Johansson, J., Kehlet, B., Logg, A., et al. (2015). The FEniCS project version 1.5. *Archive of Numerical Software*, *3*(100), 9–23. <https://doi.org/10.11588/ans.2015.100.20553>
- Barr, A. (2008). Mobile lid convection beneath Enceladus' south polar terrain. *Journal of Geophysical Research*, *113*(E7), E07009. <https://doi.org/10.1029/2008JE003114>
- Barr, A., & McKinnon, W. (2007a). Convection in Enceladus' ice shell: Conditions for initiation. *Geophysical Research Letters*, *34*(9), L09202. <https://doi.org/10.1029/2006GL028799>
- Barr, A., & McKinnon, W. (2007b). Convection in ice I shells and mantles with self-consistent grain size. *Journal of Geophysical Research*, *112*(E2), E02012. <https://doi.org/10.1029/2006JE002781>
- Běhouňková, M., Tobie, G., Choblet, G., & Čadek, O. (2013). Impact of tidal heating on the onset of convection in Enceladus's ice shell. *Icarus*, *226*(1), 898–904. <https://doi.org/10.1016/j.icarus.2013.06.033>
- Beuthe, M. (2018). Enceladus's crust as a non-uniform thin shell: I tidal deformations. *Icarus*, *302*, 145–174. <https://doi.org/10.1016/j.icarus.2017.11.009>
- Beuthe, M., Rivoldini, A., & Trinh, A. (2016). Enceladus's and Dione's floating ice shells supported by minimum stress isostasy. *Geophysical Research Letters*, *43*(19), 10088–10096. <https://doi.org/10.1002/2016GL070650>
- Blankenship, D. D., Young, D. A., Moore, W. B., & Moore, J. C. (2009). Radar sounding of Europa's subsurface properties and processes: The view from Earth. In R. T. Pallardo, W. B. McKinnon, & K. Khurana (Eds.), *Europa* (pp. 631–654). The University of Arizona Press.
- Bruzzone, L., Plaut, J. J., Alberti, G., Blankenship, D. D., Bovolo, F., Campbell, B. A., et al. (2015). Jupiter ICY Moon explorer (JUICE): Advances in the design of the radar for icy Moons (RIME). In *2015 IEEE international geoscience and remote sensing symposium (IGARSS)* (pp. 1257–1260). <https://doi.org/10.1109/IGARSS.2015.7326002>
- Buffo, J., Schmidt, B. E., Huber, C., & Walker, C. C. (2020). Entrainment and dynamics of ocean-derived impurities within Europa's ice shell. *Journal of Geophysical Research: Planets*, *125*(10), e2020JE006394. <https://doi.org/10.1029/2020je006394>
- Čadek, O., Souček, O., Běhouňková, M., Choblet, G., Tobie, G., & Hron, J. (2019). Long-term stability of Enceladus' uneven ice shell. *Icarus*, *319*, 476–484. <https://doi.org/10.1016/j.icarus.2018.10.003>
- Čadek, O., Tobie, G., Van Hoolst, T., Massé, M., Choblet, G., Lefèvre, A., et al. (2016). Enceladus's internal ocean and ice shell constrained from Cassini gravity, shape, and libration data. *Geophysical Research Letters*, *43*(11), 5653–5660. <https://doi.org/10.1002/2016GL068634>
- Castillo-Rogez, J. C., Efroimsky, M., & Lainey, V. (2011). The tidal history of Iapetus: Spin dynamics in the light of a refined dissipation model. *Journal of Geophysical Research*, *116*(E9), E09008. <https://doi.org/10.1029/2010JE003664>
- Chyba, C. F., Ostro, S. J., & Edwards, B. C. (1998). Radar detectability of a subsurface ocean on Europa. *Icarus*, *134*(2), 292–302. <https://doi.org/10.1006/icar.1998.5961>
- Corr, H., Moore, J. C., & Nicholls, K. W. (1993). Radar absorption due to impurities in Antarctic ice. *Geophysical Research Letters*, *20*(11), 1071–1074. <https://doi.org/10.1029/93GL01395>
- Culberg, R., Schroeder, D. M., & Steinbrügge, G. (2022). Double ridge formation over shallow water sills on Jupiter's moon Europa. *Nature Communications*, *13*(1), 2007. <https://doi.org/10.1038/s41467-022-29458-3>
- Culha, C., Schroeder, D. M., Jordan, T. M., & Haynes, M. S. (2020). Assessing the detectability of Europa's eutectic zone using radar sounding. *Icarus*, *339*, 113578. <https://doi.org/10.1016/j.icarus.2019.113578>
- de Pater, I., & Lissauer, J. (2001). *Planetary sciences*. Cambridge University Press.
- Di Paolo, F., Cosciotti, B., Lauro, S., Mattei, E., Vannaroni, G., Bella, F., & Pettinelli, E. (2014). Thermal and electromagnetic models for radar sounding of the Galilean satellite icy crusts. In *15th international conference on ground penetrating radar (ICGPR)* (pp. 362–366). <https://doi.org/10.1109/ICGPR.2014.6970446>
- Di Paolo, F., Lauro, S. E., Castelletti, D., Mitri, G., Bovolo, F., Cosciotti, B., et al. (2017). Radar signal penetration and horizons detection on Europa through numerical simulations. *Ieee Journal of Selected Topics in Applied Earth Observations and Remote Sensing*, *10*(1), 118–129. <https://doi.org/10.1109/JSTARS.2016.2544103>
- Dowdeswell, J. A., & Evans, S. (2004). Investigations of the form and flow of ice sheets and glaciers using radio-echo sounding. *Reports on Progress in Physics*, *67*(10), 1821–1861. <https://doi.org/10.1088/0034-4885/67/10/r03>
- Ermakov, A. I., Park, R. S., Roa, J., Castillo-Rogez, J. C., Keane, J. T., Nimmo, F., et al. (2021). A recipe for the geophysical exploration of Enceladus. *The Planetary Science Journal*, *2*(4), 157. <https://doi.org/10.3847/psj/ac06d2>
- Fox-Powell, M. G., & Cousins, C. R. (2021). Partitioning of crystalline and amorphous phases during freezing of simulated Enceladus ocean fluids. *Journal of Geophysical Research: Planets*, *126*(1), e2020JE006628. <https://doi.org/10.1029/2020JE006628>
- Glein, C. R., Postberg, F., & Vance, S. D. (2018). The geochemistry of Enceladus: Composition and controls. *Enceladus and the icy moons of Saturn*, *39*.
- Gross, G. W., Wong, P. M., & Humes, K. (1977). Concentration dependent solute redistribution at the ice–water phase boundary. III. Spontaneous convection. Chloride solutions. *The Journal of Chemical Physics*, *67*(11), 5264–5274. <https://doi.org/10.1063/1.434704>
- Hemingway, D. J., & Mittal, T. (2019). Enceladus's ice shell structure as a window on internal heat production. *Icarus*, *332*, 111–131. <https://doi.org/10.1016/j.icarus.2019.03.011>
- Hendrix, A. R., Hurford, T. A., Barge, L. M., Bland, M. T., Bowman, J. S., Brinckerhoff, W., et al. (2019). The NASA roadmap to ocean worlds. *Astrobiology*, *19*, 1–27. <https://doi.org/10.1089/ast.2018.1955>
- Higgins, P. M., Glein, C. R., & Cokell, C. S. (2021). Instantaneous habitable windows in the parameter space of Enceladus' ocean. *Journal of Geophysical Research: Planets*, *126*(11), e2021JE006951. <https://doi.org/10.1029/2021JE006951>
- Howell, S. M. (2021). The likely thickness of Europa's icy shell. *The Planetary Science Journal*, *2*(4), 129. <https://doi.org/10.3847/psj/abfe10>
- Hsu, H.-W., Postberg, F., Sekine, Y., Shibuya, T., Kempf, S., Horányi, M., et al. (2015). Ongoing hydrothermal activities within Enceladus. *Nature*, *519*(7542), 207–210. <https://doi.org/10.1038/nature14262>
- Iess, L., Stevenson, D. J., Parisi, M., Hemingway, D., Jacobson, R. A., Lunine, J. I., et al. (2014). The gravity field and interior structure of Enceladus. *Science*, *344*(6179), 78–80. <https://doi.org/10.1126/science.1250551>

- Kalousová, K., Schroeder, D. M., & Soderlund, K. M. (2017). Radar attenuation in Europa's ice shell: Obstacles and opportunities for constraining the shell thickness and its thermal structure. *Journal of Geophysical Research: Planets*, 122(3), 524–545. <https://doi.org/10.1002/2016JE005110>
- Kang, W., Mittal, T., Bire, S., Campin, J.-M., & Marshall, J. (2022). How does salinity shape ocean circulation and ice geometry on Enceladus and other icy satellites? *Science Advances*, 8(29), eabm4665. <https://doi.org/10.1126/sciadv.abm4665>
- Lobo, A. H., Thompson, A. F., Vance, S. D., & Tharimena, S. (2021). A pole-to-equator ocean overturning circulation on Enceladus. *Nature Geoscience*, 14(4), 185–189. <https://doi.org/10.1038/s41561-021-00706-3>
- Logg, A., Mardal, K. A., & Wells, G. N. (2012). *Automated solution of differential equations by the finite element method, the FEniCS book*. Springer-Verlag. <https://doi.org/10.1007/978-3-642-23099-8>
- MacGregor, J. A., Winebrenner, D. P., Conway, H., Matsuoka, K., Mayewski, P. A., & Clow, G. D. (2007). Modeling englacial radar attenuation at Siple Dome, West Antarctica, using ice chemistry and temperature data. *Journal of Geophysical Research*, 112(F3), F03008. <https://doi.org/10.1029/2006JF000717>
- Marion, G., Kargel, J., Catling, D., & Lunine, J. (2012). Modeling ammonia–ammonium aqueous chemistries in the Solar System's icy bodies. *Icarus*, 220(2), 932–946. <https://doi.org/10.1016/j.icarus.2012.06.016>
- Marusiak, A. G., Vance, S., Panning, M. P., Běhouňková, M., Byrne, P. K., Choblet, G., et al. (2021). Exploration of icy ocean worlds using geophysical approaches. *The Planetary Science Journal*, 2(4), 150. <https://doi.org/10.3847/psj/ac1272>
- Matsuoka, K., MacGregor, J. A., & Pattyn, F. (2010). Using englacial radar attenuation to better diagnose the subglacial environment: A review. In *Proceedings of the 13th international conference on ground penetrating radar (GPR)* (pp. 1–5).
- Matsuoka, K., MacGregor, J. A., & Pattyn, F. (2012). Predicting radar attenuation within the Antarctic ice sheet. *Earth and Planetary Science Letters*, 359–360, 173–183. <https://doi.org/10.1016/j.epsl.2012.10.018>
- McKay, C. P., Davila, A., Glein, C. R., Hand, K. P., & Stockton, A. (2018). Enceladus astrobiology, habitability, and the origin of life. In P. M. Schenk, R. N. Clark, C. J. A. Howett, A. J. Verbiscer, & J. H. Waite (Eds.), *Enceladus and the icy moons of Saturn* (p. 437). [https://doi.org/10.2458/azu\\_uapress\\_9780816537075-ch021](https://doi.org/10.2458/azu_uapress_9780816537075-ch021)
- McKinnon, W. B. (2005). Radar sounding of convecting ice shells in the presence of convection: Application to Europa, Ganymede, and Callisto. In *Workshop on radar investigations of planetary and terrestrial environments* (Vol. 1, p. 53).
- McKinnon, W. B. (2015). Effect of Enceladus's rapid synchronous spin on interpretation of Cassini gravity. *Geophysical Research Letters*, 42(7), 2137–2143. <https://doi.org/10.1002/2015GL063384>
- Mitri, G., & Showman, A. P. (2008). Thermal convection in ice-I shells of Titan and Enceladus. *Icarus*, 193(2), 387–396. (Saturn's Icy Satellites from Cassini). <https://doi.org/10.1016/j.icarus.2007.07.016>
- Moore, J. C. (2000). Models of radar absorption in European ice. *Icarus*, 147(1), 292–300. <https://doi.org/10.1006/icar.2000.6425>
- Moore, J. C., Reid, A. P., & Kipfstuhl, J. (1994). Microstructure and electrical properties of marine ice and its relationship to meteoric ice and sea ice. *Journal of Geophysical Research*, 99(C3), 5171–5180. <https://doi.org/10.1029/93jc02832>
- Nadeau, A., & McGehee, R. (2017). A simple formula for a planet's mean annual insolation by latitude. *Icarus*, 291, 46–50. <https://doi.org/10.1016/j.icarus.2017.01.040>
- NASEM. (2022). *Origins, worlds, and life: A decadal strategy for planetary science and astrobiology 2023–2032*. The National Academies Press. <https://doi.org/10.17226/26522>
- Ojakangas, G. W., & Stevenson, D. J. (1989). Thermal state of an ice shell on Europa. *Icarus*, 81(2), 220–241. [https://doi.org/10.1016/0019-1035\(89\)90052-3](https://doi.org/10.1016/0019-1035(89)90052-3)
- Petrenko, V. F., & Whitworth, R. W. (2002). *Physics of ice*. Oxford University Press. <https://doi.org/10.1093/acprof:oso/9780198518945.001.0001>
- Pettinelli, E., Cosciotti, B., Di Paolo, F., Lauro, S. E., Mattei, E., Orosei, R., & Vannaroni, G. (2015). Dielectric properties of Jovian satellite ice analogs for subsurface radar exploration: A review. *Reviews of Geophysics*, 53(3), 593–641. <https://doi.org/10.1002/2014RG000463>
- Phillips, R. J., Zuber, M. T., Smrekar, S. E., Mellon, M. T., Head, J. W., Tanaka, K. L., et al. (2008). Mars north polar deposits: Stratigraphy, age, and geodynamical response. *Science*, 320(5880), 1182–1185. <https://doi.org/10.1126/science.1157546>
- Picardi, G., Plaut, J. J., Biccari, D., Bombaci, O., Calabrese, D., Cartacci, M., et al. (2005). Radar soundings of the subsurface of Mars. *Science*, 310(5756), 1925–1928. <https://doi.org/10.1126/science.1122165>
- Plaut, J. J., Picardi, G., Safaeinili, A., Ivanov, A. B., Milkovich, S. M., Cicchetti, A., et al. (2007). Subsurface radar sounding of the south polar layered deposits of Mars. *Science*, 316(5821), 92–95. <https://doi.org/10.1126/science.1139672>
- Pleiner Sládková, K., Souček, O., & Běhouňková, M. (2021). Enceladus' tiger stripes as frictional faults: Effect on stress and heat production. *Geophysical Research Letters*, 48(19), e2021GL094849. <https://doi.org/10.1029/2021GL094849>
- Postberg, F., Clark, R. N., Hansen, C. J., Coates, A. J., Ore, C. M. D., Scipioni, F., et al. (2018). Plume and surface composition of Enceladus. In *Enceladus and the icy Moons of Saturn* (pp. 129–162). University of Arizona Press. [https://doi.org/10.2458/azu\\_uapress\\_9780816537075-ch007](https://doi.org/10.2458/azu_uapress_9780816537075-ch007)
- Scanlan, K. M., Young, D. A., Steinbrügge, G., Kempf, S. D., Grima, C., & Blankenship, D. D. (2021). Delay Doppler SAR focusing and quantitative quality control of the radar for Europa assessment and sounding: Ocean to near-surface (reason) sounding data product. *Ieee Journal of Selected Topics in Applied Earth Observations and Remote Sensing*, 14, 4352–4369. <https://doi.org/10.1109/jstars.2021.3072276>
- Schoenfeld, A. M., Hawkins, E. K., Soderlund, K. M., Leonard, E., & Yin, A. (2023). Particle entrainment and rotating convection in Enceladus' ocean. *Communications Earth & Environment*, 4(1), 28. <https://doi.org/10.1038/s43247-023-00674-z>
- Schroeder, D. M., Bingham, R. G., Blankenship, D. D., Christianson, K., Eisen, O., Flowers, G. E., et al. (2020). Five decades of radioglaciology. *Annals of Glaciology*, 61(81), 1–13. <https://doi.org/10.1017/aog.2020.11>
- Schroeder, D. M., Grima, C., & Blankenship, D. D. (2016). Evidence for variable grounding-zone and shear-margin basal conditions across Thwaites Glacier, West Antarctica. *Geophysics*, 81(1), WA35–WA43. <https://doi.org/10.1190/geo2015-0122.1>
- Seu, R., Phillips, R. J., Biccari, D., Orosei, R., Masdea, A., Picardi, G., et al. (2007). SHARAD sounding radar on the Mars Reconnaissance Orbiter. *Journal of Geophysical Research*, 112(E5), E05S05. <https://doi.org/10.1029/2006JE002745>
- Soderlund, K. M., Kalousová, K., Buffo, J. J., Glein, C. R., Goodman, J. C., Mitri, G., et al. (2020). Ice–Ocean exchange processes in the Jovian and Saturnian satellites. *Space Science Reviews*, 216(5), 1–57. <https://doi.org/10.1007/s11214-020-00706-6>
- Souček, O., Běhouňková, M., Čadek, O., Hron, J., Tobie, G., & Choblet, G. (2019). Tidal dissipation in Enceladus' uneven, fractured ice shell. *Icarus*, 328, 218–231. <https://doi.org/10.1016/j.icarus.2019.02.012>
- Souček, O., Běhouňková, M., Schroeder, D., Wolfenbarger, N., Kalousová, K., Steinbrügge, G., & Soderlund, K. (2022). Radar attenuation in Enceladus' ice shell: Obstacles and opportunities for constraining shell thickness, chemistry, and thermal structure [Dataset]. Zenodo. <https://zenodo.org/record/7428498#.Y5csTNLMJkg>
- Stillman, D. E., MacGregor, J. A., & Grimm, R. E. (2013). Electrical response of ammonium-rich water ice. *Annals of Glaciology*, 54(64), 21–26. <https://doi.org/10.3189/2013AoG64A204>
- Tajeddine, R., Soderlund, K. M., Thomas, P. C., Helfenstein, P., Hedman, M. M., Burns, J. A., & Schenk, P. M. (2017). True polar wander of Enceladus from topographic data. *Icarus*, 295, 46–60. <https://doi.org/10.1016/j.icarus.2017.04.019>

- Thomas, P. C., Burns, J. A., Helfenstein, P., Squyres, S., Veverka, J., Porco, C., et al. (2007). Shapes of the Saturnian icy satellites and their significance. *Icarus*, *190*(2), 573–584. <https://doi.org/10.1016/j.icarus.2007.03.012>
- Thomas, P. C., Tajeddine, R., Tiscareno, M. S., Burns, J. A., Joseph, J., Lored, T. J., et al. (2016). Enceladus's measured physical libration requires a global subsurface ocean. *Icarus*, *264*, 37–47. <https://doi.org/10.1016/j.icarus.2015.08.037>
- Vance, S. D., Journaux, B., Hesse, M., & Steinbrügge, G. (2021). The salty secrets of icy ocean worlds. *Journal of Geophysical Research: Planets*, *126*(1), e2020JE006736. <https://doi.org/10.1029/2020je006736>
- van Hoolst, T., Baland, R.-M., & Trinh, A. (2016). The diurnal libration and interior structure of Enceladus. *Icarus*, *277*, 311–318. <https://doi.org/10.1007/s11214-007-9202-6>
- Waite, J. H., Glein, C. R., Perryman, R. S., Teolis, B. D., Magee, B. A., Miller, G., et al. (2017). Cassini finds molecular hydrogen in the Enceladus plume: Evidence for hydrothermal processes. *Science*, *356*(6334), 155–159. <https://doi.org/10.1126/science.aai8703>
- Weller, M. B., Fuchs, L., Becker, T. W., & Soderlund, K. M. (2019). Convection in thin shells of icy satellites: Effects of latitudinal surface temperature variations. *Journal of Geophysical Research: Planets*, *124*(8), 2029–2053. <https://doi.org/10.1029/2018JE005799>
- West, R., Gim, Y., Tan, I., & Hawkins, D. (2017). Radar ambiguities and signal processing design tradeoffs in the REASON radar sounder.
- Wolfenbarger, N. S., Buffo, J. J., Soderlund, K. M., & Blankenship, D. D. (2022). Ice shell structure and composition of ocean worlds: Insights from accreted ice on Earth. *Astrobiology*, *22*(8), 937–961. <https://doi.org/10.1089/ast.2021.0044>
- Wolfenbarger, N. S., Fox-Powell, M. G., Buffo, J. J., Soderlund, K. M., & Blankenship, D. D. (2022). Compositional controls on the distribution of brine in Europa's ice shell. *Journal of Geophysical Research: Planets*, *127*(9), e2022JE007305. <https://doi.org/10.1029/2022je007305>
- Zeng, Y., & Jansen, M. F. (2021). Ocean circulation on Enceladus with a high-versus low-salinity Ocean. *The Planetary Science Journal*, *2*(4), 151. <https://doi.org/10.3847/psj/ac1114>

## Erratum

In the originally published version of this article, the department name “Mathematical Institute” was omitted from the first author affiliation. The affiliation has been corrected, and this may be considered the authoritative version of record.